Universiteit
Leiden
The Netherlands

Exploring strange new worlds with high-dispersion spectroscopy

Serindag, D.B.

Citation
Serindag, D. B. (2022, October 6). *Exploring strange new worlds with high-dispersion spectroscopy*. Retrieved from https://hdl.handle.net/1887/3466049

Version:	Publisher's Version
License:	Licence agreement concerning inclusion of doctoral thesis in the Institutional Repository of the University of Leiden
Downloaded from:	https://hdl.handle.net/1887/3466049

Note: To cite this publication please use the final published version (if applicable).

Chapter 4

A search for protoplanets around the young star HD 169142 using molecule mapping

Dilovan B. Serindag, Callum S. Griffiths, Ignas A. G. Snellen, and Rico Landman
To be submitted

Abstract

Context. Protoplanetary disks exhibit a range of substructures such as rings, gaps, and spirals. An important goal is to link these structures to the possible protoplanets that shape them. One such system is HD 169142, which shows two rings among which near-infrared high-contrast images have revealed several candidate protoplanets.

Aims. We searched for spectral signatures of these protoplanets in the HD 169142 system and, in particular, for the candidate object at an in-disk orbital distance of 38 AU. We aimed to confirm the presence of this planet, and to constrain the chemical composition of its atmosphere.

Methods. We used the molecule mapping technique on K-band integral field spectroscopic data ($\mathcal{R} \sim 5000$) taken with the SINFONI instrument on the Very Large Telescope, utilizing a grid of BT-Settl spectral models. The spectral contribution of the host star was removed from each spatial position, after which the residual spectra were cross-correlated with the models. Sensitivity limits were determined by injecting artificial planets using the same model grid.

Results. No spectral signatures were detected around HD 169142 at the locations of the candidate protoplanets. The injection and recovery analysis indicated that these observations are sensitive to a planet with mass $\gtrsim$7.3 $M_{\rm J}$ for a system age of 5–11 Myr at the location of the best candidate previously identified.

Conclusions. The observations presented here appear to be insufficiently sensitive to confirm or reject the main protoplanet candidate at 38 AU, which was suggested to have a mass $\lesssim$6 $M_{\rm J}$. Additional integral field spectroscopic observations will enhance the recoverability of any planet signal. However, since previous analysis suggested the planet is likely accreting, extinction by surrounding dust may complicate spectral analysis at medium resolution, and necessitate high-resolution studies. A similar scenario was suggested to explain the non-detection with molecule mapping of the protoplanets in the PDS 70 system. We estimate about 52 min of observing time is needed on ERIS, the upcoming high-dispersion successor to SINFONI, to reach the reported mass upper limit of the putative planet in HD 169142. The same result would require about 1 min of observing time on HARMONI, the planned optical/near-infrared integral field spectrograph for the Extremely Large Telescope.

4.1 Introduction

Many protoplanetary disks show substructures such as rings, gaps, and spirals that could indicate the presence of protoplanets (e.g., ALMA Partnership et al. 2015; Andrews et al. 2016; Andrews 2020, and the references therein). Finding and characterizing the responsible planets, as has been done for the PDS 70 system (e.g., Keppler et al. 2018; Haffert et al. 2019), constitutes an important step in better understanding planet formation. For instance, the chemical composition of their atmospheres is expected to trace the formation and early evolution of planets. Various factors, including formation location, migration, and gas versus solid accretion history are expected to affect bulk quantities such as relative elemental abundances and metallicity (e.g., Madhusudhan 2019, and the references therein). Planet formation theories incorporating these different factors provide predictions that can be tested by spectroscopic atmospheric observations (e.g., Line et al. 2021). Accessing and analyzing the atmospheric compositions of as complete a population as possible, across various orbital distances and planet ages, is thus critical to refining our understanding of the processes by which planets and their atmospheres form and evolve.

High contrast imaging enables the study of an exoplanet population largely inaccessible using other detection and characterization techniques. Whereas the transit and radial velocity methods for exoplanet analysis are inherently biased to close-in planets, spatially resolving exoplanets and their host stars is most feasible for relatively wide orbits ($\gtrsim$10 AU). At the moment, the number of imaged planets stands in the dozens, mainly because only very young planets that are still warm from their formation are bright enough to be detected. This is many fewer than the thousands provided by transit and radial velocity studies. Nonetheless, the ability to probe planets on wide orbits as well as young planets, possibly still undergoing formation, is invaluable.

Based on the cross-correlation technique pioneered by Snellen et al. (2010) to identify molecular signatures in high-resolution exoplanet spectra, Hoeijmakers et al. (2018b) developed "molecule mapping" for use with medium-resolution ($\mathcal{R} \sim 10^3$) integral field spectroscopy (IFS). First, the stellar spectral contribution is removed from each spatial location in the data set. By subsequently cross-correlating spectral templates of various molecules with the spectra at each spatial location, they measured the signatures of CO and H_2O in the atmosphere of the young (24 Myr; Bell et al. 2015) widely-orbiting (10 AU; Lacour et al. 2021) gas-giant planet β Pictoris b, and broadly constrained the planetary effective temperature and surface gravity by comparing the cross-correlation strengths retrieved for a grid of BT-Settl spectral models. Similar studies were

subsequently performed for other young directly-imaged planets, detecting CO and H_2O in both HR 8799 b (Petit dit de la Roche et al. 2018) and in HIP 65426 b (Petrus et al. 2021).

The HD 169142 system is estimated to be 5–11 Myr old, and consists of a gas-rich disk surrounding a 1.65–2 $M_\odot$ Herbig Ae/Be star (Gratton et al. 2019, and the references therein). VLA (Osorio et al. 2014), ALMA (Fedele et al. 2017), and near-infrared polarimetric observations (Quanz et al. 2013; Monnier et al. 2017; Pohl et al. 2017; Bertrang et al. 2018) all revealed two rings spanning approximately 0.″17–0.″28 (ring 1) and 0.″48–0.″64 (ring 2)[1]. Some studies proposed that disk structures such as the annular gap between rings 1 and 2 and a radial gap in ring 1 may imply the presence of planets in HD 169142 (Fedele et al. 2017; Bertrang et al. 2018). Other near-infrared observations (Biller et al. 2014; Reggiani et al. 2014) reported possible point-sources within 0.″2, but subsequent observations spanning multiple years by Ligi et al. (2018) and Gratton et al. (2019) could not confirm the existence of these features.

Gratton et al. (2019) expanded the near-infrared data set first presented by Ligi et al. (2018), and searched for persistent flux excesses in low-resolution ($\mathcal{R} \sim$ 30–50) IFS data in the Y-J (0.95–1.35 μm) and Y-H (0.95–1.65 μm) bands taken with the SPHERE instrument on the Very Large Telescope (VLT). In these data with epochs spanning three years, Gratton et al. (2019) found four persistent, extended flux sources that orbit the star with roughly Keplerian velocities: blob A at 13.5 AU, located in between the star and ring 1; blobs B and C within ring 1, at 21.4 AU and 23.1 AU, respectively; and blob D at 36.4 AU, within the annular gap between rings 1 and 2. Combining simultaneous observations with IRDIS on VLT/SPHERE in the $K1$ (2.09 μm) and $K2$ (2.25 μm) bands, Gratton et al. (2019) suggested that the relatively flat, reddish blob-to-star spectral contrasts are indicative of extincted, dust-scattered stellar light. They also found evidence for spiral arm structures within ring 1. Taken together, Gratton et al. (2019) proposed that the Y-J-H-band detection of blob D is starlight reflecting off an accretion flow associated with a nearby planet. They noted that the $K2$-band detection of blob D is spatially offset compared to its location in the Y-J-H band, which may indicate that the longer wavelength observations probed the planet's photosphere. In such a scenario, the putative planet would be responsible for carving the gap between rings 1 and 2, as well as exciting the spiral arms within ring 1. Using various metrics (photometry, inferred Hill radius, spiral arm separation, spiral arm pitch angle, disk gap size), they constrained the mass of this putative planet at 38 AU to $\lesssim$6 M_J, with a

[1]We adopt the ring nomenclature and spatial extents from Gratton et al. (2019).

best estimate of 2.2 $M_{\rm J}$.

In this chapter, we searched for spectral signatures at and around the location of blob D in medium-resolution IFS data taken using SINFONI on the VLT utilizing the molecule mapping technique. We cross-correlated exoplanet spectral templates with the spectra at each spatial location in our IFS observations. We also performed a sensitivity analysis of our data by injecting and recovering synthetic planet signals at the same on-sky orbital separation expected for blob D. In Section 4.2 we present our SINFONI data of HD 169142, and outline the processing techniques we applied to mitigate stellar and telluric contamination. We outline our methodology for searching for planet signals and performing the sensitivity analysis in Sections 4.3 and 4.4, respectively, and present the associated results in Section 4.5. We discuss these results and conclude in Section 4.6.

4.2 Integral field spectroscopic data of HD 169142

4.2.1 Data acquisition and characteristics

We observed[2] HD 169142 with the SINFONI integral field spectrograph (Eisenhauer et al. 2003; Bonnet et al. 2004) mounted on the Cassegrain focus of the Very Large Telescope UT4. Thirty-two observations were taken on 17 August 2018 and 16 observations on 18 August 2018, each consisting of 15 exposures of 4 s. The K-band grating was selected to provide a wavelength coverage of 1.93–2.47 μm at a resolving power of $\mathcal{R} \sim 5000$ (60 km s^{-1}) with a pixel sampling of $2.45{\times}10^{-4}$ μm.

The spectrograph pre-optics were set for a field of view (FOV) of $0\farcs8 \times 0\farcs8$, with an orientation fixed at a position angle of 0° such that North and East point up ($+y$ direction) and left ($-x$ direction), respectively. In this setup, the SINFONI image slicer cuts along the East-West axis, producing 32 slices with a height of 25 mas. Each slice is then spatially sampled along the East-West axis by 64 pixels of size 12.5 mas. The spatial resolution is therefore 25 mas × 12.5 mas in declination and right ascension, respectively.

[2]ESO program ID: 0101.C-0582(A); PI: Snellen

4.2.2 Data reduction

We used the EsoRex pipeline (Freudling et al. 2013) to perform the initial data reduction on the bias-corrected SINFONI observations of HD 169142, including bad pixel masking, dark frame corrections, flat fielding, distortion corrections, and wavelength calibration. From each observation's raw data, the pipeline constructed a data cube of $2216 \times 64 \times 64$ voxels[3] in λ, y, and x, respectively. Note the y-axis (declination) has been over-sampled by a factor of two.

The edges of the spectral axis contain bad frames as well as frames that are heavily contaminated by telluric features, so we retained only those frames with wavelengths 2.08–2.45 μm. To regain the native spatial resolution of 25 mas along the y-axis, we averaged adjacent pairs of rows in each wavelength frame. The spatial edges of each frame also contain rows and columns of bad spaxels[4]. We therefore removed the two top- and bottom-most rows and the four left- and right-most columns from each wavelength frame.

In each observation, the stellar photocenter is spatially offset from the center of the FOV by varying amounts. To spatially recenter each cube, we first generated a white-light image based on the median along the spectral axis. We then determined the spatial location of the stellar photocenter by fitting a two-dimension Gaussian to the 231 pixels surrounding the flux peak in the white-light image. Based on this spatial location, we linearly interpolated each frame in the given cube such that the spatial center corresponds to the fitted stellar photocenter. In the re-gridding, we preserved the 25 mas $\times$ 12.5 mas spatial resolution.

To verify the quality of the wavelength calibration for each cube, we cross-correlated the central 231 spaxels with a vacuum-wavelength ESO SkyCalc model (Noll et al. 2012; Jones et al. 2013) of the Earth's transmission spectrum, and determined the velocity offsets corresponding to the maximum cross-correlation values. The wavelength drift of each cube was calculated as the median velocity offset over these central spaxels. Over all observations, there is a $\approx$31 km s^{-1} redshift compared to the vacuum rest frame. To correct these offsets, we used a cubic spline to Doppler shift the spaxels in a given cube to the vacuum rest frame. The top left panel of Figure 4.1 shows the white light image of HD 169142 after this rest frame correction, calculated by median-combining the cubes of the individual observations and then taking the median flux along the wavelength axis.

[3]Data cube elements
[4]Spectrum for a given spatial position

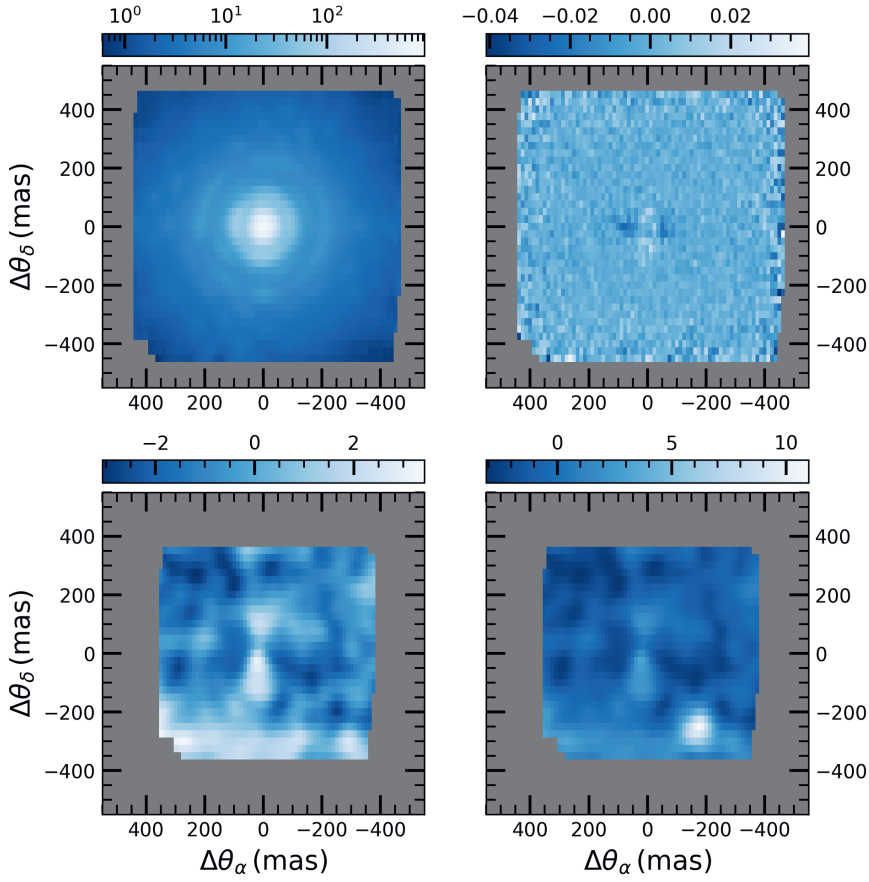

Figure 4.1. *Top left panel*: white light image of HD 169142 generated from the master cube of rest-frame-corrected observations. The colorbar flux units are arbitrary. *Top right panel*: white light image generated from the master cube of all observations after the removal of ten PCA components. The colorbar flux units are arbitrary. *Bottom left panel*: S/N image at $v = 0$ km s^{-1} for the cross-correlation of the $T_{\rm eff} = 1800$ K, $\log g = 4.0$ BT-Settl model with the PCA10 master cube. *Bottom right panel*: S/N image at $v = 0$ km s^{-1} for the cross-correlation of the $T_{\rm eff} = 1800$ K, $\log g = 4.0$ BT-Settl model with the PCA10 master cube, injected with a 1.6-$R_{\rm J}$ planet at $(\Delta\theta_\alpha, \Delta\theta_\delta) = (-179, -260)$ mas.

4.2.3 Removal of stellar and telluric contamination

To facilitate the retrieval of planetary spectral signals, further processing steps are necessary to remove the contributions of the host star and the Earth's atmosphere. Here, we loosely followed the recipe for molecule mapping presented in Hoeijmakers et al. (2018b). We first constructed a reference stellar spectrum for each cube by individually normalizing the central 45 spaxels by their total flux counts before taking the median in each wavelength bin. In calculating the median, we excluded values more than six standard deviations from the bin median. This reference spectrum serves as a template for the contributions from the stellar point-spread-function (PSF) and telluric absorption.

We divided the spaxels in each cube by that cube's reference stellar spectrum to determine the relative spectral contribution as a function of wavelength at each spatial position. To isolate low-frequency deviations (e.g., from quasi-static speckles) while preserving any potential high-frequency planetary signal, we performed a low-pass Gaussian filter with a FWHM of 20 pixels ($\approx 5{\times}10^{-3}$ μm) on the relative spectral contribution at each spaxel. We then subtracted from each spaxel the reference stellar spectrum scaled by that spaxel's low-frequency relative spectral contribution. The resulting flux residuals for each spaxel should subsequently be largely devoid of low-frequency spectrally- and spatially-dependent contributions of the stellar PSF and telluric absorption.

To attempt to clean any remaining stellar and telluric noise, we performed a 6σ clipping of each spaxel, masked any outliers, and, for regions that are well sampled, subsequently replaced their value by the mean value of the adjacent ten voxels in the spectrum. We then projected each cube onto a two-dimensional matrix where each column is a different spaxel. On these matrices we performed a principle component analysis (PCA) using the singular value decomposition technique (e.g., de Kok et al. 2013). Removing increasing numbers of principle components from the matrix decreases the correlated noise. For each cube, we performed the PCA iteratively to generate ten new cubes, each with an additional principle component removed.

4.2.4 Combining observations

To maximize any potential planet signal in our set of SINFONI observations, we stacked the residual flux cubes for all 48 observations. The stacking was performed by taking the median for each voxel across the set of observations. The residual flux cubes were stacked for each PCA iteration separately, resulting in 11 master cubes for PCA iterations 0–10. As an example, the top right panel

of Figure 4.1 shows the white light image generated from the master cube for the PCA10 case.

4.3 Search for planet signals

We searched for planetary spectral signatures in the SINFONI data by cross-correlating BT-Settl (CIFIST) models[5] (Allard et al. 2011, 2012, 2013) with each spaxel in the 11 residual flux cubes (Section 4.2.4) on velocities (v) spanning -2000 to $+2000$ km s^{-1} in steps of 10 km s^{-1}. The result is a set of 11 cross-correlation cubes in v, y, and x for each model. We restricted ourselves to solar metallicity models with $T_{\rm eff} = 1200$–4000 K and $\log g = 2.5$–5.5. To maximize the retrieval of any potential planet signal, prior to cross-correlation we broadened the BT-Settl models to $\mathcal{R} = 5000$ to match the SINFONI resolving power and performed a high-pass filtering to mimic our treatment of the data.

To further enhance the signal recoverability of possible planetary signals, we convolved each velocity frame in the cross-correlation cubes with a two-dimensional Gaussian. This accounts for the fact that any planet signal, like that of the star, should be spatially extended by the PSF of the imaging system. The widths of the convolution kernel along the x- and y-axes were determined by fitting a two-dimensional Gaussian to the stellar PSF in the rest-frame-corrected white light image of the star, shown in the top left panel of Figure 4.1 and described in Section 4.2.2. The Gaussian convolution kernel was truncated at three times the width along each axis.

To quantify the strength of correlation peaks relative to the surrounding noise, we divided the cross-correlation values in each spaxel by the standard deviation of the cross-correlation values in that spaxel with velocities $|v| > 500$ km s^{-1}, so as to avoid the contribution of any potential planet signal. We thereby converted the cross-correlation cubes to signal-to-noise ratio (S/N) cubes. The bottom left panel of Figure 4.1 shows an example image at $v = 0$ km s^{-1} from the S/N cube generated from the cross-correlation of the $T_{\rm eff} = 1800$ K, $\log g = 4.0$ BT-Settl model with the PCA10 master cube. While there is clearly no statistically-significant peak in this case, for comparison, the bottom right panel of Figure 4.1 shows how the S/N image would look with a 1.6-$R_{\rm J}$ planet added at $(\Delta\theta_\alpha, \Delta\theta_\delta) = (-179, -260)$ mas. The artificial signal in the bottom right corner of this panel is clearly visible.

[5]Retrieved from
http://svo2.cab.inta-csic.es/theory/newov2/index.php?models=bt-settl-cifist

4.4 Injection–recovery tests of synthetic planet signals

We also evaluated the recoverability of planetary signals in the SINFONI data by performing injection–recovery tests with synthetic planet signals. To simulate the planetary spectrum, we used the same BT-Settl models described in Section 4.3, broadened to $\mathcal{R} = 5000$ to match the resolving power of SINFONI. To ensure accurate flux levels for the synthetic planet signals, we generated a planet PSF by scaling the stellar PSF profile by the wavelength-dependent luminosity contrast between the simulated planet and the host star HD 169142. We determined the stellar PSF profile for each wavelength frame of each observation by fitting a two-dimensional Gaussian to the 861 voxels about the stellar photocenter. The luminosity contrast for a synthetic planet of radius R_p and effective temperature $T_\mathrm{eff,p}$ was calculated as the flux ratio of the BT-Settl model spectrum for $T_\mathrm{eff,p}$ to the blackbody spectrum for $T_{\mathrm{eff},\star} = 7500$ K, scaled by $(R_\mathrm{p}/R_\star)^2$ with $R_\star = 1.59\ R_\odot$ (Blondel & Djie 2006). We adopted $\log g = 4.0$ for all synthetic planets.

To inject a synthetic planet signal into a given observation, we truncated the planet PSF beyond 3σ from the peak and added it to the corresponding rest-frame-corrected data cube. After performing this injection for each observation in our data set, we ran the injected data cubes through the same reduction procedure outlined in Sections 4.2.3 and 4.2.4 to remove stellar and telluric contamination. We recovered the injected signal by cross-correlating the master cubes with the broadened, filtered version of the BT-Settl model used to generate the synthetic planet signal, and then performing a two-dimensional Gaussian convolution as described in Section 4.3. Since we wanted to quantify the recoverability even in the weak signal cases, we calculated the S/N value for each voxel as the difference between the injected and uninjected cross-correlation values for that voxel, normalized by the standard deviation of the cross-correlation values for $|v| > 500$ km s^{-1} in the corresponding uninjected spaxel. We adopted the maximum value on the S/N cube within one voxel ($\Delta v = 10$ km s^{-1}, $\Delta y = 25$ mas, $\Delta x = 12.5$ mas) of the injection location as the recovered S/N.

4.5 Results

4.5.1 Non-detection of planet signal

We examined the S/N cubes described in Section 4.3 for statistically significant peaks near the expected radial velocity and spatial location of blob D. We set the velocity range rather wide at $|v| \leq 100$ km s^{-1}, which easily accommodates the contributions of the heliocentric motion of the VLT in the direction of HD 169142 ($+22$ km s^{-1}), the heliocentric radial velocity of the system (-3 ± 2 km s^{-1}; Dunkin et al. 1997a,b), and the expected orbital velocity of the planet along our line of sight (± 1 km s^{-1}). This latter value was calculated as the line-of-sight Keplerian velocity assuming a circular orbit, a system inclination of 13°, a stellar mass of 1.65 $M_{\odot}$ (Blondel & Djie 2006), and an in-disk orbital distance for blob D of 36.4 AU (Gratton et al. 2019). To determine the spatial position of blob D in our data, we deprojected the most recent on-sky position of blob D reported in Table 3 of Gratton et al. (2019) into the disk plane, advanced the orbital position to the epoch of our SINFONI observations using the in-disk orbital speed presented in Table 7 of the same work, and re-projected the updated position to the sky plane. We estimated the error in this updated position by performing the same procedure on a sample of 10^5 positions and orbital velocities drawn from normal distributions with spreads corresponding to the reported errors in Gratton et al. (2019), and taking the standard deviation of the resulting distribution. We defined the spatial bounds for our search as the spaxels containing x and y values within ± 6 standard deviations of the expected on-sky position of blob D. These velocity and spatial bounds also easily incorporate the slightly offset location of the putative planet. No peaks with S/N > 4 were found within these bounds in the S/N cubes for any of the BT-Settl models. Similar searches at the locations of blobs B and C did not reveal any peaks with S/N > 4 either, while the corresponding search at the location of blob A was inconclusive due to the presence of strong residual stellar contamination.

4.5.2 Injection–recovery tests

Using the injection–recovery procedure described in Section 4.4, we determined the sensitivity of our data and reduction method to recovering planet signals at the on-sky orbital distance of blob D (316 mas). We injected synthetic planet signals assuming various planet effective temperatures and radii to probe different planet–star luminosity contrasts. For each $T_{\mathrm{eff,p}}$–R_{p} combination, we

performed the injection–recovery procedure at $v = 0$ km s^{-1} and three spatial locations with a constant on-sky offset of 315.6 mas and position angles offset by 90°, 180°, and 270° from the expected 34.6°. We averaged the maximum recovered S/N for these three cases to determine a single recoverable S/N for each contrast. The spread in S/N values relative to the average value was always $\lesssim$30%. These average values are presented in Figure 4.2. Each panel shows the sensitivity of our SINFONI data and reduction procedure for different values of planet radius (y-axis) and effective temperature (x-axis). The color gradient indicates the average recovered S/N, with blue shades corresponding to S/N < 5 and red shades corresponding to S/N > 5. For typical planet radii of 1.6–1.8 $R_{\rm J}$, we are only sensitive to effective temperatures $\gtrsim$1600 K.

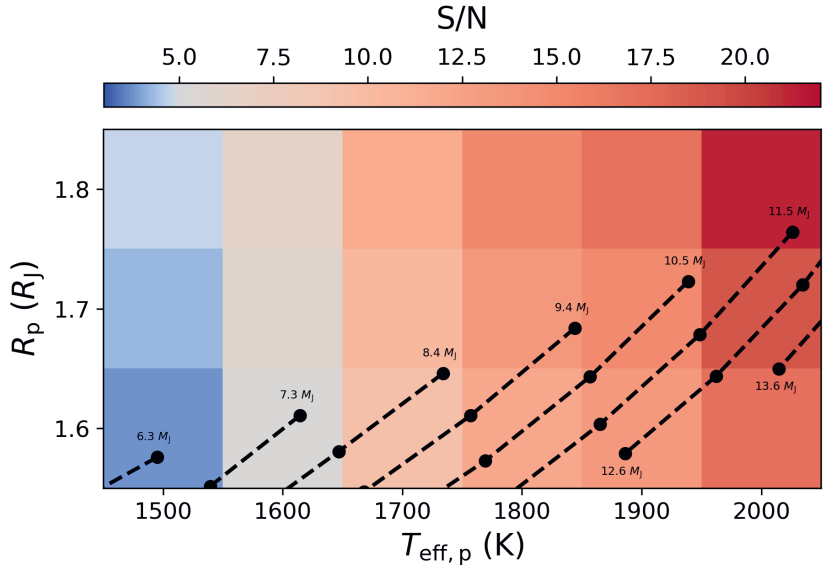

Figure 4.2. Recoverability of injected planet signals in our SINFONI data set at the on-sky distance of blob D. Each panel corresponds to a different effective temperature and radius, and the color coding indicates the recovered S/N value, averaged across the three injection locations. The color gradient breaks at S/N = 5, which we adopted as the threshold for a robust detection. The evolutionary tracks from Phillips et al. (2020) are plotted in black for various planet masses for the 5–11 Myr age of HD 169142.

4.6 Discussion and conclusions

Using the molecule mapping technique with BT-Settl spectral models, we were unable to confirm the presence of the putative planet in the SINFONI data at or near the persistent flux feature labeled blob D by Gratton et al. (2019), or indeed at any of the other blob locations reported therein. Despite allowing rather generous velocity and spatial bounds, no cross-correlation peaks with S/N $>$ 4 were found near the expected location of the putative planet. In light of our sensitivity analysis in Section 4.5.2, this result is not necessarily unexpected.

To link the sensitivity of our data and methodology at the various $T_{\rm eff,p}$ and $R_{\rm p}$ plotted in Figure 4.2 to physically-realistic planet cases, we overplotted the model evolutionary tracks from Phillips et al. (2020) for low-mass objects in black. We only show those time steps (black circles) within the 5–11 Myr age range of HD 169142. Each curve corresponds to a different object mass, and demonstrates the cooling and contraction of planets in the immediate aftermath of formation. Based on the transition of the recovered S/N values from less than to greater than 5 around 1500–1600 K, we conclude that our analysis is sensitive to masses $\gtrsim$7.3 $M_{\rm J}$ near the location of blob D in the HD 169142 system. We are thus insensitive to the putative planet mass proposed in Gratton et al. (2019). They constrained the planet mass to $\lesssim$6 $M_{\rm J}$, with a best estimate of 2.2 $M_{\rm J}$.

Potentially further complicating the retrieval of planetary spectral signals is the scenario proposed by Gratton et al. (2019) that the persistent blob D found in their IFS observations is stellar light reflected off an accretion flow feeding the nearby putative planet. While we were unable to find evidence in our master cubes of Brackett γ emission indicative of accretion, such a scenario may suggest surrounding material that could obscure the spectral lines of the planet's photosphere, as seems to be the case for PDS 70 b. The PDS 70 system is young (5.4 Myr; Müller et al. 2018) and contains two widely-orbiting protoplanets PDS 70 b and PDS 70 c at 21 AU and 35 AU, respectively (Keppler et al. 2018; Müller et al. 2018; Haffert et al. 2019). Both planets have been shown to be actively accreting based on spatially-resolved detections of Hα emission (Wagner et al. 2018; Haffert et al. 2019). Subsequent analysis of PDS 70 b by Cugno et al. (2021) was unable to detect spectral signatures of H_2O, CO, or CH_4 in SINFONI data using similar reduction and cross-correlation techniques to our study. They suggested that dust extinction is the likely cause of the non-detection of molecular features at medium spectral resolution, one source of which may be a dusty shell enveloping the planet. As a remedy, they noted observations at higher spectral resolution should enable a greater line-to-

continuum contrast, and thereby enhance the detectability of extincted spectral signatures.

Probing the spectroscopic signature of the putative protoplanet near blob D in HD 169142 therefore requires additional observations, ideally at higher spectral resolution. Although the SINFONI instrument has been decommissioned, the upcoming VLT instrument ERIS will incorporate the refurbished SINFONI IFS, upgraded to enable high-dispersion ($\mathcal{R} = 8000$) observations. We can estimate how much more observing time on ERIS is required from the S/N value in Figure 4.2 for 1.6 $R_{\rm J}$ and 1500 K, which are very similar to the radius and $T_{\rm eff}$ values predicted by the Phillips et al. (2020) models for a 6.3 $M_{\rm J}$ planet. Based on the retrieved S/N value of 3.8 from the injection–recovery tests, achieving a S/N of 5 at this flux contrast with the higher ERIS resolving power would require 1.1× as much observing time, or about 52 min. In contrast, only about 1 min of observing time would be required to reach a S/N of 5 using the highest-dispersion setting ($\mathcal{R} = 18,000$) on HARMONI, the planned optical/near-infrared IFS for the Extremely Large Telescope. These estimates should be taken as lower limits on the observing time, as ∼6 $M_{\rm J}$ is the upper limit for the putative planet.

Acknowledgments

D.B.S., I.A.G.S., and R.L. acknowledge support from the European Research Council under the European Union's Horizon 2020 research and innovation program under grant agreement No. 694513. This research has made use of the Spanish Virtual Observatory (http://svo.cab.inta-csic.es) supported from Ministerio de Ciencia e Innovación through grant PID2020-112949GB-I00.